

Analysis of Doubly Corrugated Spoof Surface Plasmon Polariton (DC-SSPP) Structure With Sub-Wavelength Transmission at THz Frequencies

Zhao Xu, Kyungjun Song, and Pinaki Mazumder, *Fellow, IEEE*

Abstract—Devices utilizing spoof surface plasmon polariton (SSPP) effect in the terahertz (THz) domain has attracted increasing attention because such devices can be potentially used in fast signal processing and storages. In this paper, we present a comprehensive mathematical model of the doubly corrugated SSPP (DC-SSPP) structure derived from full-field analysis. Based on the proposed model, a complete characterization of the structure is carried out and properties such as dispersion relationships and S-parameters are obtained. The results show the existence of slow light modes in the DC-SSPP structure. Discrete sub-wavelength transmission bands, and sometimes sharp transmission peaks with strong EM field localization can also be achieved under certain device designs. They are compared with the simulation results obtained from the CST software package developed by Computer Simulation Technology AG. The validation as well as limitations of the derived results is also discussed in detail.

Index Terms—Dispersion relationship, doubly corrugated spoof surface plasmon polariton (DC-SSPP), full-field analysis, S-parameters.

I. INTRODUCTION

AS A RESULT of their potential applications in domains like astronomical remote sensing, biomedical imaging, harmful chemical detection, and ultrafast computer logic circuit [1]–[3], there has been an increasing interest in developing terahertz (THz) devices and circuits in recent years. Unlike conventional millimeter devices, THz devices utilize higher frequency, typically 0.1–10 THz, to realize higher bit sampling rate and broader bandwidth. On the other hand, by implementing simple waveguide structures, THz devices have the potential of eliminating the bulk and complexity of quantum cascade laser (QCL) devices working in far-infrared spectrum. Using mature nanofabrication techniques such as deep reactive ion etching (DRIE) and lithography, electroplating, and molding (LIGA), active THz devices, such as THz sources and amplifiers, have been realized and studied by several researchers [4]–[6]. For passive THz devices, design and fabrication of guiding structures, focusing elements and frequency selective filters have also gained considerable attention [2], [7]–[9].

Manuscript received October 17, 2011; revised January 07, 2012; accepted January 23, 2012. This work is supported in part by the Army Research Office under Grant W911NF-10-1-0229 and also by the MURI grant W911NF-11-1-0024.

The authors are with the Department of Electrical Engineering and Computer Science, University of Michigan, MI 48109 USA (e-mail: .mazum@eecs.umich.edu).

Color versions of one or more of the figures in this paper are available online at <http://ieeexplore.ieee.org>.

Digital Object Identifier 10.1109/TTHZ.2012.2188558

Conventional index-guiding methods, such as plastic ribbons and sapphire fibers, are not suitable for THz waveguiding given its high signal power loss in the frequency range [7], [10], [11]. As a result, structures employing spoof surface plasmon polariton (SSPP) modes are proposed as a low loss and low dispersion alternative. SSPP modes are bound electromagnetic waves which propagate on the periodically corrugated metal surface at frequencies outside the conventional plasmonic spectrum of metals. The transverse mode profile of the SSPP modes mimics those of the real plasmonic waves of metal in optical frequencies, which gives rise to a strongly localized energy distribution near the metal-dielectric interface. As a result, sub-wavelength transmission, which is the low-loss transmission of EM signals through structural features (holes, slits, etc.) with smaller-than-wavelength dimensions, can be realized. Wang, *et al.* have first demonstrated the possibility of low-loss, dispersion-free THz waveguiding using metal wires surrounded by dielectrics [12]. Pendry *et al.* then proposed the structure with 2-D surface modifications, namely by introducing periodic holes, grooves and dimples into the metal-dielectric interface of the device, to realize sub-wavelength transmission of THz electromagnetic waves [13]. Transmission, guiding and focusing of THz waves has then been demonstrated in numerous works that followed [8], [9], [14]–[17].

By introducing 1-D periodic grooves into smooth waveguide structure on opposing metal-dielectric interfaces, in this paper a doubly corrugated SSPP (DC-SSPP) waveguide is realized. This structure has strong confinement of THz waves inside the groove region at resonance, and therefore is suitable for various applications such as narrow bandpass filters and active THz switches [18], [19]. In our previous work, the DC-SSPP structure has been studied by using various simulation packages. Elaborate software, such as HFSS and MEEP, has been utilized to demonstrate the structure's great potential in frequency-selective, sub-wavelength signal transmission in the THz domain.^{1, 2} Accurate as they are, these CAD tools usually require long simulation time and thus are better limited to the final stage of device design. In contrast, a full mathematical analysis of the SSPP structure is helpful as it is derived from the physics of the structure, and is usually more time efficient. Although works of other research groups have shown partial/full mathematic analysis of periodic corrugated structures aimed at THz applications similar to our design [15], [20]–[23], such analysis on a sub-wavelength DC-SSPP THz waveguiding structure is yet to appear.

¹Ansoft HFSS, Ansys Inc., Pittsburg, PA.

²MEEP (MIT Electromagnetic Equation Propagation), Massachusetts Institute of Technology, Boston, MA.

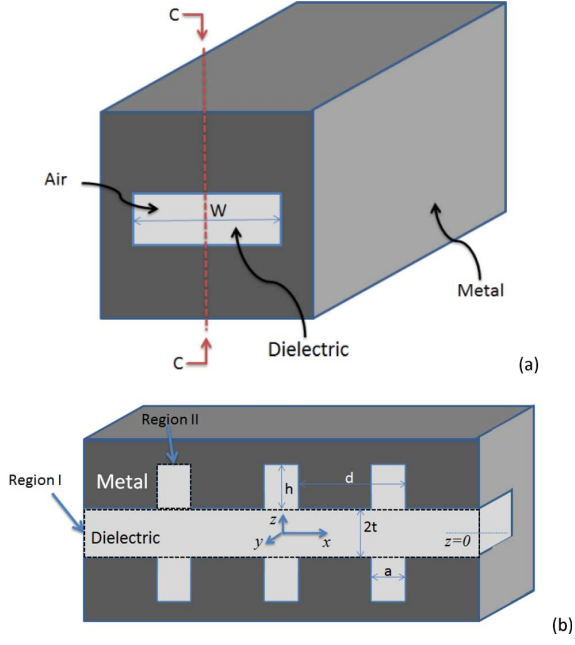


Fig. 1. Geometry of the structure under consideration: (a) front view and (b) cross-section view at plane defined by C-C.

In this paper, we perform full-field analysis of the DC-SSPP waveguiding structure and based on that, we derive the mathematical solutions to the dispersion relationships of different SSPP modes. A scattering matrix method is then employed and the transmission properties of the structure are obtained. Properties of such structure, such as the existence of the slow-light SSPP mode and discrete transmission bands in the frequency domain are demonstrated. To our best knowledge, it is the first work of its kind to solve the full dispersion map as well as transmission properties of the sub-wavelength DC-SSPP THz structures at once, using full physics analysis and calculations. In addition, simulations using CST software are performed for the purpose of comparison.³

This paper is organized as follows. In Section II, the expression for dispersion relationships of various modes of the DC-SSPP structure is derived. The difference between symmetric and anti-symmetric SSPP modes in the derivation will be demonstrated in detail. In Section III, the dispersion relationships are treated as inputs based on which a full scattering matrix iterative methodology is employed to obtain the transmission property of the structure. Results of both calculations will be demonstrated and compared with results obtained using CST simulation software in Sections IV and V. In Section VI, detailed discussion regarding the interpretation, validity and limitations of our calculation will be provided. In Section VII, we will summarize the calculation and present our conclusion.

II. CALCULATION OF DISPERSION RELATIONSHIP

The DC-SSPP structure under investigation consists of dielectric materials surrounded by metal, and is illustrated in Fig. 1. The structure is in general divided into two regions:

Region I is the waveguiding dielectric section without corrugations, and Region II represents the periodic groove areas. In our convention, d is the period of the grooves, a and h are the width and depth of the grooves, respectively, $2t$ is the height of the smooth part of the structure, and W represents the width of the structure. The coordinate system is also shown in Fig. 1, with $z = 0$ positioned at the midpoint of the structure and $x = 0$ at the center of one of the grooves.

Based on Maxwell's equations, mathematical expressions of the EM fields are explicitly written out for both Regions I and II. As is common in the treatment of structures with similar geometry, the x -dependency of the EM field is best expressed by a Floquet mode expansion due to the periodic nature of the structure [15], [20]–[24]. The mirror symmetry of the structure also indicates, that the field distribution along z -axis must be either symmetric or anti-symmetric. In other words, the z -dependency of mode distributions needs to be in the form of either *cosine* or *sine* functions.

In our convention, we refer to the symmetry of our modes using the y -polarized H field. Therefore for anti-symmetric modes, the EM fields in both regions are expressed as follows.

In Region I

$$\begin{bmatrix} H_x^I \\ H_y^I \\ H_z^I \end{bmatrix} = \sum_{n=-\infty}^{\infty} \rho_n e^{jk_{x,I}^{(n)}x} \begin{bmatrix} j \frac{k_y k_{z,I}^{(n)}}{v_y^2} \cos(k_y y) \sin(k_{z,I}^{(n)} z) \\ \sin(k_y y) \sin(k_{z,I}^{(n)} z) \\ \frac{k_y k_{z,I}^{(n)}}{v_y^2} \cos(k_y y) \cos(k_{z,I}^{(n)} z) \end{bmatrix} \quad (1)$$

$$\begin{bmatrix} E_x^I \\ E_y^I \\ E_z^I \end{bmatrix} = \frac{1}{\omega \epsilon} \frac{k_0^2}{v_y^2} \sum_{n=-\infty}^{\infty} \rho_n e^{jk_{x,I}^{(n)}x} \times \sin(k_y y) \begin{bmatrix} -jk_{z,I}^{(n)} \cos(k_{z,I}^{(n)} z) \\ 0 \\ -k_{x,I}^{(n)} \sin(k_{z,I}^{(n)} z) \end{bmatrix}. \quad (2)$$

In Region II

$$\begin{bmatrix} H_x^{II} \\ H_y^{II} \\ H_z^{II} \end{bmatrix} = \begin{bmatrix} -\frac{k_y k_{z,II}}{v_y^2} (A^+ e^{jk_{z,II}z} + A^- e^{-jk_{z,II}z}) \cos(k_y y) \sin(k_{x,II}x) \\ (A^+ e^{jk_{z,II}z} + A^- e^{-jk_{z,II}z}) \sin(k_y y) \cos(k_{x,II}x) \\ j \frac{k_y k_{z,II}}{v_y^2} (A^+ e^{jk_{z,II}z} - A^- e^{-jk_{z,II}z}) \cos(k_y y) \cos(k_{x,II}x) \end{bmatrix} \quad (3)$$

$$\begin{bmatrix} E_x^{II} \\ E_y^{II} \\ E_z^{II} \end{bmatrix} = \frac{1}{\omega \epsilon} \frac{k_0^2}{v_y^2} \sin(k_y y) \times \begin{bmatrix} k_{z,II} (A^+ e^{jk_{z,II}z} - A^- e^{-jk_{z,II}z}) \cos(k_{x,II}x) \\ 0 \\ -jk_{x,II} (A^+ e^{jk_{z,II}z} + A^- e^{-jk_{z,II}z}) \sin(k_{x,II}x) \end{bmatrix}. \quad (4)$$

In the above expressions, $k_{x,I}^{(n)}$ and $k_{z,I}^{(n)}$ denote the wavevectors of the n th-order Floquet mode along x -axis and z -axis in

³CST, Computer Simulation Technology AG, Framingham, MA.

Region I, and ρ_n signifies its amplitude coefficient. Correspondingly, $k_{x,II}$ and $k_{z,II}$ denote the wavevectors along the two axis in Region II. Other variables are defined as follows:

$$\begin{aligned} v_y^2 &= k_0^2 - k_y^2 = \left(k_{x,I}^{(n)}\right)^2 + \left(k_{z,I}^{(n)}\right)^2 \quad \text{in Region I} \\ v_y^2 &= k_0^2 - k_y^2 = k_{x,II}^2 + k_{z,II}^2 \quad \text{in Region II, and} \\ k_y &= \frac{m\pi}{W}, \quad m = 1, 2, \dots \\ k_{x,II} &= \frac{l\pi}{a}, \quad l = 0, 1, 2, \dots \end{aligned}$$

By expressing the EM field distributions using above expressions, these modes automatically satisfy the boundary conditions that the tangential E field and normal H field shall vanish at all dielectric-metal interfaces. In addition, boundary conditions at the interface between Region I and Region II requires the transverse EM field to be continuous

$$\begin{aligned} H_y^I &= H_y^{II}: \sum_{n=-\infty}^{\infty} \rho_n \sin(k_y y) \sin\left(k_{z,I}^{(n)} t\right) e^{jk_{x,I}^{(n)} x} \\ &= \left(A^+ e^{jk_{z,II} t} + A^- e^{-jk_{z,II} t}\right) \sin(k_y y) \cos(k_{x,II} x) \end{aligned} \quad (5)$$

$$\begin{aligned} E_x^I &= E_x^{II}: -\frac{1}{\omega\epsilon} \frac{k_0^2}{v_y^2} \sum_{n=-\infty}^{\infty} j k_{z,I}^{(n)} \rho_n \sin(k_y y) \cos\left(k_{z,I}^{(n)} t\right) e^{jk_{x,I}^{(n)} x} \\ &= \frac{1}{\omega\epsilon} \frac{k_0^2}{v_y^2} k_{z,II} \left(A^+ e^{jk_{z,II} t} - A^- e^{-jk_{z,II} t}\right) \\ &\quad \times \sin(k_y y) \cos(k_{x,II} x). \end{aligned} \quad (6)$$

In our structure a is small compared to the wavelength of the propagating field. As a result higher order modes in Region II as denoted by the expression $k_{x,II} = (l\pi)/a, l = 0, 1, 2, \dots$ are always evanescent in all other directions. It is therefore safe to assume that only the lowest order of the $k_{x,II}$ modes is significant in our calculation. In that condition if we denote $B^+ = A^+ e^{jk_{z,II} t}$ and $B^- = A^- e^{-jk_{z,II} t}$, for any given order of $k_y = (m\pi)/W, m = 1, 2, \dots$, the above equations can be simplified as

$$\sum_{n=-\infty}^{\infty} \rho_n \sin\left(k_{z,I}^{(n)} t\right) e^{jk_{x,I}^{(n)} x} = B^+ + B^- \quad (7)$$

$$-\sum_{n=-\infty}^{\infty} j k_{z,I}^{(n)} \rho_n \cos\left(k_{z,I}^{(n)} t\right) e^{jk_{x,I}^{(n)} x} = k_{z,II} (B^+ - B^-). \quad (8)$$

By integrating both sides of (7) and (8) for one period along x -axis, and by imposing boundary conditions such that tangential E field must vanish at the horizontal surface at $z = t$ in interval $x \in [a, d]$, the following equation can be obtained:

$$j \sum_{n=-\infty}^{\infty} \frac{k_{z,II}}{k_{z,I}^{(n)}} |T_n|^2 \tan\left(k_{z,I}^{(n)} t\right) (B^+ - B^-) = (B^+ + B^-) \quad (9)$$

with

$$|T_n|^2 = \left| \sqrt{\frac{1}{ad}} \int_0^a e^{jk_{x,I}^{(n)} x} dx \right|^2 = \frac{a}{d} \left| \text{sinc}\left(\frac{k_{x,I}^{(n)}}{2} a\right) \right|^2. \quad (10)$$

To solve for B^+ and B^- , another equation is needed. Such equation can be obtained when we consider another boundary condition, which is that the tangential E field must vanish at the bottom of the groove

$$B^+ e^{jk_{z,II} h} - B^- e^{-jk_{z,II} h} = 0, \quad (11)$$

By combining (9) and (11), a matrix equation is obtained for variables B^+ and B^- . In this manner, the problem is formulated into an eigenvalue equation problem. In order for the equation to have non-trivial solutions, we need to force the determinant of the matrix to be 0. As a result, the dispersion relationship for the anti-symmetric modes of the DC-SSPP structure could be finally obtained as

$$1 - \sum_{n=-\infty}^{\infty} \frac{k_{z,II}}{k_{z,I}^{(n)}} |T_n|^2 \tan\left(k_{z,I}^{(n)} t\right) \tan(k_{z,II} h) = 0. \quad (12)$$

Equation (12) looks similar to the dispersion relationships solved by other works as presented in [20], [22], [23], however is intrinsically different. In fact, anti-symmetric modes can only exist in DC-SSPP structures and therefore is a unique feature of such geometry. They are best characterized by the degeneracy of their dispersion curves, as will be shown and discussed in detail in Section IV.

Other than the anti-symmetric modes, the doubly corrugated SSPP structure can also support symmetric modes, as expressed by following mode expressions.

In Region I

$$\begin{bmatrix} H_x^I \\ H_y^I \\ H_z^I \end{bmatrix} = \sum_{n=-\infty}^{\infty} \rho_n e^{jk_{x,I}^{(n)} x} \begin{bmatrix} j \frac{k_y k_{x,I}^{(n)}}{v_y^2} \cos(k_y y) \cos\left(k_{z,I}^{(n)} z\right) \\ \sin(k_y y) \cos\left(k_{z,I}^{(n)} z\right) \\ -\frac{k_y k_{z,I}^{(n)}}{v_y^2} \cos(k_y y) \sin\left(k_{z,I}^{(n)} z\right) \end{bmatrix} \quad (13)$$

$$\begin{bmatrix} E_x^I \\ E_y^I \\ E_z^I \end{bmatrix} = \frac{1}{\omega\epsilon} \frac{k_0^2}{v_y^2} \sum_{n=-\infty}^{\infty} \rho_n e^{jk_{x,I}^{(n)} x} \times \sin(k_y y) \begin{bmatrix} j k_{z,I}^{(n)} \sin\left(k_{z,I}^{(n)} z\right) \\ 0 \\ -k_{x,I}^{(n)} \cos\left(k_{z,I}^{(n)} z\right) \end{bmatrix}. \quad (14)$$

In Region II, see (15) and (16), shown at the bottom of the next page.

Following the same procedure as in the case of anti-symmetric modes, the dispersion relationship of the symmetric modes can be obtained by solving the following equation:

$$1 + \sum_{n=-\infty}^{\infty} \frac{k_{z,II}}{k_{z,I}^{(n)}} \frac{|T_n|^2}{\tan\left(k_{z,I}^{(n)} t\right)} \tan(k_{z,II} h) = 0. \quad (17)$$

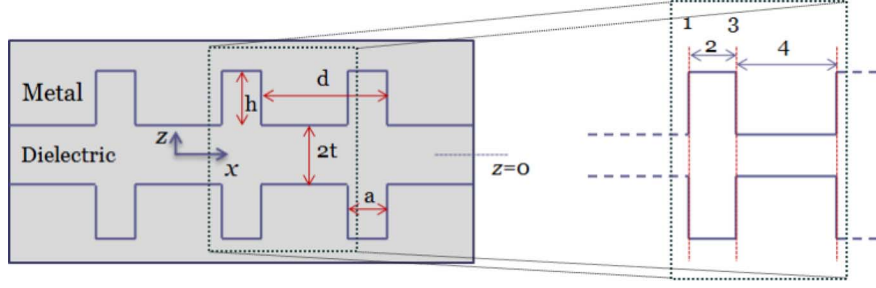


Fig. 2. Break-down of a single “cell” of the DC-SSPP structure into four sections as explained in the .

Compared with (12), the solutions of (17) feature dispersion curves that closely resemble those of other corrugated structures. For example, the dispersion relationships of single-sided SSPP structure are very similar in general shape [20], [22], [23]. The detailed analysis of such modes and their significance in real applications will also be discussed in Section IV.

III. CALCULATION OF TRANSMISSION PROPERTIES

As an important part in the complete characterization of the DC-SSPP structure, the transmission properties contain the information of the frequency-dependent reflectance and transmittance (conventionally denoted as R and T) of the SSPP device. We use scattering matrix method to study such properties and an iterative algorithm is employed.

We first divide each of the single “cells” (meaning one periodic unit which repeats itself to form the whole structure) in x -direction into four sections, as shown in Fig. 2.

To be explicit, the four sections are: 1) the abrupt change from the narrow part to the wide part of the structure which can be understood as a step junction; 2) the straight wide part (containing the groove), which is an analogy to a smooth transmission line; 3) the abrupt change from the wide part back to the narrow part of the structure, which is another step junction; and 4) the smooth narrow part, which again, is an analogy to a homogeneous transmission line.

The treatment of periodic microwave structures using scattering/transmission matrices (S/T -matrices) are studied in detail by [25]. Here a similar approach is used to describe the S -matrices of each section of the single cell as delineated above. Unlike the classical waveguide modes used in [25], in our case the mode profile inside the structure is described by SSPP modes as solved in Section II. Accordingly, the mode coupling efficiency across the abrupt structural changes needs significant modifications.

By using the same notations as in [25], H is defined as the *mode matching efficiency* across the boundary and is expressed as

$$H = \frac{\int_{-(t+h)}^{t+h} \langle h_2 | h_1 \rangle dz}{\int_{-(t+h)}^{t+h} \langle h_1 | h_1 \rangle dz} \quad (18)$$

In the above expressions, h_1 and h_2 denotes the transverse magnetic fields on the two sides of the boundary and $\langle \rangle$ denotes an inner product. In our case, the mode distributions are obtained by combining (7), (8) and (11) for anti-symmetric modes, and their equivalent for symmetric modes. If we assume only the lowest order Floquet mode is significant, which is usually the case since higher order modes are in most circumstances evanescent waves, after some straightforward yet tedious mathematical deductions, we can have

$$H_y^I = 2\sqrt{\frac{a}{d}} T_0^* \frac{k_{z,II}}{k_{z,I}^{(0)}} \frac{A \sin(k_{z,II} h)}{\cos(k_{z,I}^{(0)} t)} \sin(k_{z,I}^{(0)} z) e^{jk_{x,I}^{(0)} x} \quad (19)$$

in Region I

$$H_y^{II} = 2A \cos(k_{z,II} [z - (t + h)]) \quad (20)$$

in Region II for anti-symmetric modes, and

$$H_y^I = -2\sqrt{\frac{a}{d}} T_0^* \frac{k_{z,II}}{k_{z,I}^{(0)}} \frac{A \sin(k_{z,II} h)}{\sin(k_{z,I}^{(0)} t)} \cos(k_{z,I}^{(0)} z) e^{jk_{x,I}^{(0)} x} \quad (21)$$

in Region I

$$H_y^{II} = 2A \cos(k_{z,II} [z - (t + h)]) \quad (22)$$

$$\begin{bmatrix} H_x^{II} \\ H_y^{II} \\ H_z^{II} \end{bmatrix} = \begin{bmatrix} -\frac{k_y k_{z,II}}{v_y^2} (A^+ e^{jk_{z,II} z} + A^- e^{-jk_{z,II} z}) \cos(k_y y) \sin(k_{x,II} x) \\ (A^+ e^{jk_{z,II} z} + A^- e^{-jk_{z,II} z}) \sin(k_y y) \cos(k_{x,II} x) \\ j \frac{k_y k_{z,II}}{v_y^2} (A^+ e^{jk_{z,II} z} - A^- e^{-jk_{z,II} z}) \cos(k_y y) \cos(k_{x,II} x) \end{bmatrix} \quad (15)$$

$$\begin{bmatrix} E_x^{II} \\ E_y^{II} \\ E_z^{II} \end{bmatrix} = \frac{1}{\omega \epsilon} \frac{k_0^2}{v_y^2} \sin(k_y y) \begin{bmatrix} k_{z,II} (A^+ e^{jk_{z,II} z} - A^- e^{-jk_{z,II} z}) \cos(k_{x,II} x) \\ 0 \\ -jk_{x,II} (A^+ e^{jk_{z,II} z} + A^- e^{-jk_{z,II} z}) \sin(k_{x,II} x) \end{bmatrix}. \quad (16)$$

in Region II for symmetric modes. In the above expressions, A is the amplitude constant, and $*$ denotes the complex conjugate.

Take Section I as an example. Using (18), H can be calculated for anti-symmetric mode and for symmetric modes, respectively, as shown in (23) and (24) at the bottom of the page.

The S-matrix of Section I can then be written out using the following formulas. Here we use the same notations as in the [25]. Y_2 is calculated as the effective admittance and is a function of the *mode matching efficiency* H and the admittance value Y_{01} . Y_{01} and Y_{02} on the other hand, are the characteristic admittance of the waveguide on both sides of the interface, respectively

$$\begin{aligned} S_{22} &= T_2^{-1}(Y_{02} + Y_2)^{-1}(Y_{02} - Y_2)T_2 \\ S_{12} &= H(S_{22} + I) \\ S_{21} &= Q_2^{-1}S_{12}^T Q_1 \\ S_{11} &= HS_{21} - I. \end{aligned} \quad (25)$$

For further information regarding definitions of different notations and the calculation of the above expressions, one can refer to [25]. Following the same approach, the S-matrices of all the other sections can be as well calculated.

In order to combine S-matrices of four sections together, as well as to obtain the S-matrix of the whole structure from that of the single cell, there are in general two approaches. One is to transform the S-matrices into transmission or transfer matrices (T-matrices), which can be simply multiplied together to get the overall T-matrix (and henceforth the S-matrix of the whole structure). This approach is conceptually straightforward; however it could introduce significant numerical errors to the end result when there are evanescent wave terms in the unit T-matrices.

An alternative approach is to use the S-matrices themselves in the entire calculation. Unlike the T-matrices, since mathematically the S-matrices are not directly stackable, there is no closed-form solution to the end result. Instead, an iterative algorithm is needed to solve the problem. This approach is well explained and the mathematical form of the algorithm is explicitly given in several literatures [26], [27]. It is proved to be effective in terms of eliminating the numerical instabilities as stated above. Therefore, this iterative approach is used throughout our work reported here to obtain the overall S-matrix of the DC-SSPP structures.

IV. DISPERSION RELATIONSHIP: RESULT AND COMPARISON

A DC-SSPP THz structure with dimensions $d = 100 \mu\text{m}$, $a = 10 \mu\text{m}$, $h = 80 \mu\text{m}$, $t = 33.33 \mu\text{m}$, and $W = 300 \mu\text{m}$ (from now on referred to as DC-SSPP-1 structure) is considered in our calculation. For meanings of different notations, please refer to Fig. 1. We use MATLAB as the software environment for our entire analytical calculation⁴. The dispersion curves of the first and second symmetric mode, as well as the first anti-symmetric mode of the structure are shown in Fig. 3. Due to the nonzero width of the structure in y -direction, a cut-off frequency of 0.5 THz is presented. One must note that such cut-off wavelength should not be used as a benchmark in the description of sub-wavelength transmission, since in the THz domain the conventional index-guiding mechanism of a waveguide does not apply.

Fig. 3(a) shows our calculation result, while in Fig. 3(b) simulation result obtained by CST simulation software are included for comparison. As can be observed, the general shape of the dispersion curves of both approaches coincides with each other very well. Quantitatively, there are small yet observable differences in the two curves. The reason behind such discrepancies will be discussed in detail in Section VI.

In Fig. 3(a), the dispersion curve of the 1st symmetric mode resembles closely the shape of the surface plasmon mode on a smooth metal-dielectric interface. It is therefore an SSPP mode, and its resonance frequency is by principle determined by the dimensions of the periodic structure. By examining (12) and (17), the plasmonic resonance frequency of the first modes can be estimated to the first order by the following expression:

$$f_{pl} = \sqrt{\left(\frac{c}{4nh}\right)^2 + f_y^2}, \quad f_y = \frac{c}{2nW}. \quad (26)$$

In (26), f_y stands for the cut-off frequency due to the nonzero y -dimension of the structure, n is the refractive index of the dielectric material ($n = 1$ with air filling in this case), and c is the speed of light. For the DC-SSPP-1 structure, f_{pl} is calculated to be 1.06 THz. In our analytical model, the same resonance frequency at 1.025 THz can be observed in Fig. 3(a), which is a close agreement with the estimation. This resonance frequency corresponds to a wavelength of $\lambda = 293 \mu\text{m}$, which is much larger than the height of the waveguide ($2t = 66.7 \mu\text{m}$).

⁴Matlab, Mathworks Inc., Natick, MA.

For anti-symmetric mode

$$H = \frac{\frac{a}{d}|T_0|^2 \left(\frac{2k_{z,II} \sin(k_{z,II}h)}{k_{z,I}^{(0)} \cos(k_{z,I}^{(0)}t)} \right)^2 \left(t - \frac{1}{2k_{z,I}^{(0)}} \sin(2k_{z,I}^{(0)}t) \right)}{4h + \frac{2}{k_{z,II}} \sin(2k_{z,II}h) + \frac{a}{d}|T_0|^2 \left(\frac{2k_{z,II} \sin(k_{z,II}h)}{k_{z,I}^{(0)} \cos(k_{z,I}^{(0)}t)} \right)^2 \left(t - \frac{1}{2k_{z,I}^{(0)}} \sin(2k_{z,I}^{(0)}t) \right)} \quad (23)$$

For anti-symmetric mode

$$H = \frac{\frac{a}{d}|T_0|^2 \left(\frac{2k_{z,II} \sin(k_{z,II}h)}{k_{z,I}^{(0)} \sin(k_{z,I}^{(0)}t)} \right)^2 \left(t + \frac{1}{2k_{z,I}^{(0)}} \sin(2k_{z,I}^{(0)}t) \right)}{4h + \frac{2}{k_{z,II}} \sin(2k_{z,II}h) + \frac{a}{d}|T_0|^2 \left(\frac{2k_{z,II} \sin(k_{z,II}h)}{k_{z,I}^{(0)} \sin(k_{z,I}^{(0)}t)} \right)^2 \left(t + \frac{1}{2k_{z,I}^{(0)}} \sin(2k_{z,I}^{(0)}t) \right)} \quad (24)$$

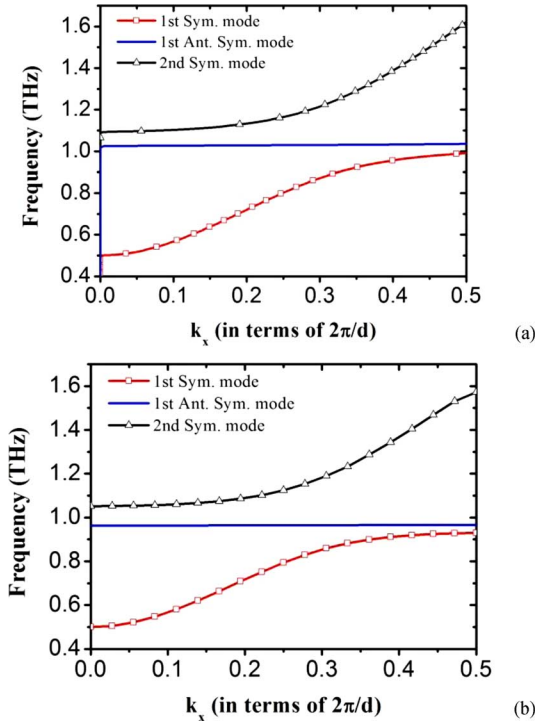


Fig. 3. Dispersion relationship of the DC-SSPP-1 structure using the stated dimensions: (a) as simulated using our analytical model and (b) as obtained using CST software package. In both figures, the red line with square data markers denotes the first symmetric mode, the blue line with triangle data markers represents the first anti-symmetric mode, and the black line the second symmetric mode.

Therefore this mode represents a sub-wavelength resonance of the structure.

From Fig. 3(a) a slow-light mode can also be observed, which is the 1st anti-symmetric mode (as represented by the blue line). This mode has a nearly flat dispersion curve, which suggests the existence of a pass-band very sharp and narrow. However, on the downside, this flatness also indicates a mode group velocity of almost 0, which will severely lower the energy coupling efficiency into and out of the structure.

This mode has a great potential to be used in applications such as passive frequency filters and active switches. Nonetheless, to really take advantage of it, we need its dispersion relationship to have a reasonable slope and curvature. This is realized by adjusting the dimensions of the DC-SSPP structure. To illustrate our point, we use an example with the following dimensions: $d = 100 \mu\text{m}$, $a = 10 \mu\text{m}$, $h = 30 \mu\text{m}$, $t = 33.33 \mu\text{m}$, and $W = 300 \mu\text{m}$ (from now on referred to as DC-SSPP-2 structure). The new dispersion relationships of the same three SSPP modes are shown in Fig. 4. Compared to the DC-SSPP-1 structure, the only change here is to replace $h = 80 \mu\text{m}$ with $h = 30 \mu\text{m}$.

From Fig. 4, an increase in the slope of the first anti-symmetric mode can be observed. Furthermore, in this case, even the second symmetric mode becomes reasonably narrow band, which is a good demonstration of the influence of geometrical dimensions on the spectral responses of DC-SSPP structures. Again, comparison between the curves obtained by MATLAB and CST shows small yet discernible differences, especially when it comes close to the resonance frequencies. The reason

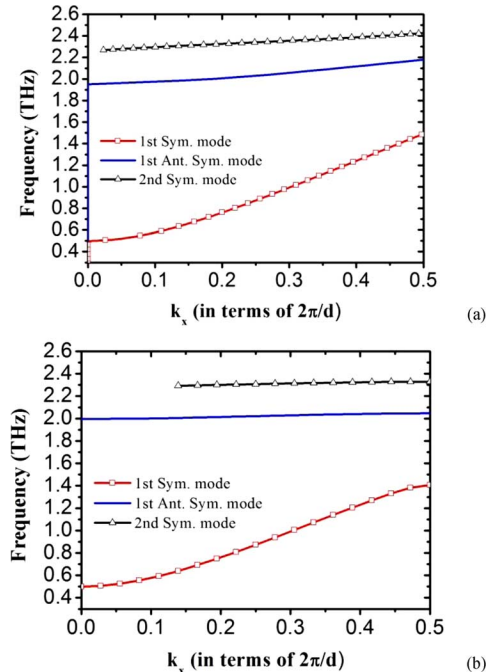


Fig. 4. Dispersion relationship of the DC-SSPP-2 structure using the stated dimensions: (a) as simulated using our analytical model and (b) as obtained using CST software package. In both figures, the red line with square data markers denotes the first symmetric mode, the blue line with triangle data markers represents the first anti-symmetric mode, and the black line the second symmetric mode.

why our MATLAB calculation is slightly more error-prone when near resonance will be discussed later in Section VI.

From both Figs. 3 and 4, it is observed that frequency selective modes are the higher order modes above the first band-gap. The fundamental mode (1st symmetric mode in our context) on the other hand, is always occupying a broad pass-band directly above cut-off and hence is less useful in any frequency sensitive designs. In that sense, knowledge of the higher order SSPP modes is of more significance than that of the fundamental one.

Regarding this demand, our simulation is able to draw the dispersion map of all the higher order modes of the DC-SSPP structure, which is included here in Fig. 5. It shows the dispersion curves of the first 5 modes of the DC-SSPP-1 structure from which the complex nature of those modes can be clearly seen. In general, those higher order SSPP modes can be categorized into two kinds. One kind consists of modes that are separated by the band-gaps, as a natural solution to (12) and (17). They are also the same higher order modes as we referred to in all previous figures and analysis. The other kind, on the other hand, consists of modes that are merely pushed up from lower orders as higher y -direction orders are used in calculation (represented by larger m values in the expression $k_y = (m\pi)/(W)$, $m = 1, 2, \dots$). Therefore they are almost clones in shape to the lower order modes and can be easily recognized.

Since the mode solutions with different y -dimension orders are themselves independent, modes from different y -orders can intersect with each other without affect the accuracy of our calculations. However, if one is to use any of those modes in real applications, cares must be taken such that the EM field can be selectively coupled into the specific mode as one desires.

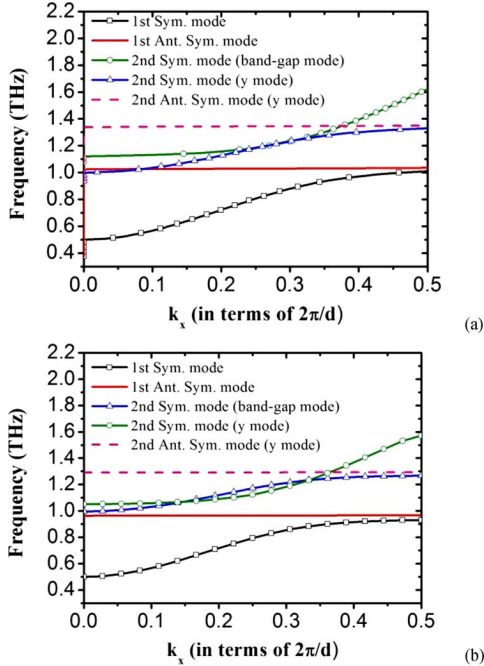


Fig. 5. Dispersion map of the first 5 modes of the DC-SSPP-1 structure: (a) as simulated using our analytical model and (b) as obtained using CST software package.

V. TRANSMISSION PROPERTIES: RESULT AND COMPARISON

Using DC-SSPP-1 structure, the S-parameters for the 1st symmetric mode of the structure as obtained using our analytical model is presented in Fig. 6(a). The structure under consideration has 5 sets of grooves. The curve can be divided in general into two parts, namely the pass-band on the left half and the stop-band on the right half of the graph. When the frequency is in the pass band, Fabry–Perot effect caused by multiple reflections from different groove edges gives rise to the multiple ripple features that can be observed on both S_{21} and S_{22} curves. For comparison, the same S parameter curves are obtained using CST simulation packages and the result is included here in Fig. 6(b). As we can see, the two curves are almost identical. There is a small yet discernible difference between frequency values where total reflection begins to appear. The detail of this discrepancy shall be included in discussion in Section VI.

In Fig. 6(c) details of the S-parameters near the start of the second transmission band near $f = 1.10$ THz is shown. This transmission band corresponds to the second symmetric mode as is shown in the dispersion relationship curves in Fig. 3(a). On the other hand, the first pass band in Fig. 6(a) and (b) corresponds to the first symmetric mode of the structure, as can be clearly observed.

We did the same simulation on the DC-SSPP-2 structure. Similarly, five sets of grooves are considered in the calculation. The simulation result is shown in Fig. 7.

Similarly, the S curves in Fig. 7 can be divided into sections. From 0.5 THz to about 1.4 THz we observe the first pass-band, where the ripple features on the curve suggests multiple reflections. The broad peak in the S_{22} parameter is a sign of the first band-gap, which is centered at 1.5 THz. The second band-gap starts at around 2.0 THz, as represented by the sudden growth of

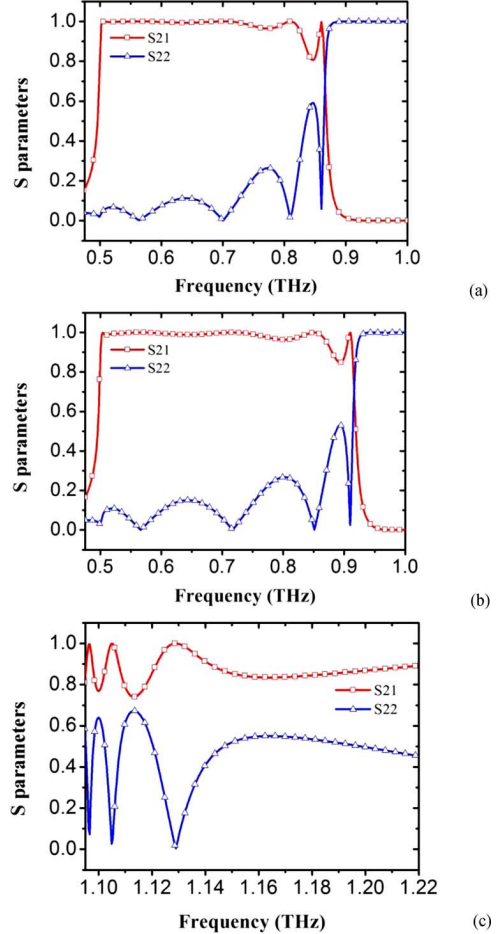


Fig. 6. S-parameters of the DC-SSPP-1 structure: (a) as simulated using our analytical model, (b) as obtained using CST software package, and (c) details at the start of the second transmission band around $f = 1.10$ THz. In these figures, the red line with square data markers denotes the S_{21} parameter, and the blue line with triangle data markers represents the S_{22} parameter.

S_{22} to 1 and the abrupt drop of S_{21} to 0. When compared with the CST simulation result, it is also quite obvious that the two curves agree with each other with reasonable accuracy. There is a very narrow transmission peak at around 2.28 THz, corresponding to the flat 2nd symmetric mode. In Fig. 7(c) a blow-up of this narrow peak in transmission band is shown. It can be seen that this peak in fact consists of multiple small transmission lines, which is again caused by the Fabry-Perot effect of multiple reflections. The multiple features of the transmission curve match perfectly with the dispersion relationship we have calculated for the same structure, which is shown in Fig. 4(a).

In both structures, discrete transmission bands are observed in sub-wavelength frequencies. Those transmission bands/peaks near SSPP resonance are at 1.10 THz ($\lambda = 272 \mu\text{m}$) and 2.28 THz ($\lambda = 132 \mu\text{m}$) for DC-SSPP-1 and DC-SSPP-2 structures, respectively, both of which are multiples of the waveguide height. One can also observe from (26) that the width W of the waveguide determines the cut-off frequency of the DC-SSPP structure by affecting f_y . When W increases, the cut-off wavelength f_y decreases and so will the SSPP resonance frequency, resulting in even larger passable wavelength for the same height of the waveguide.

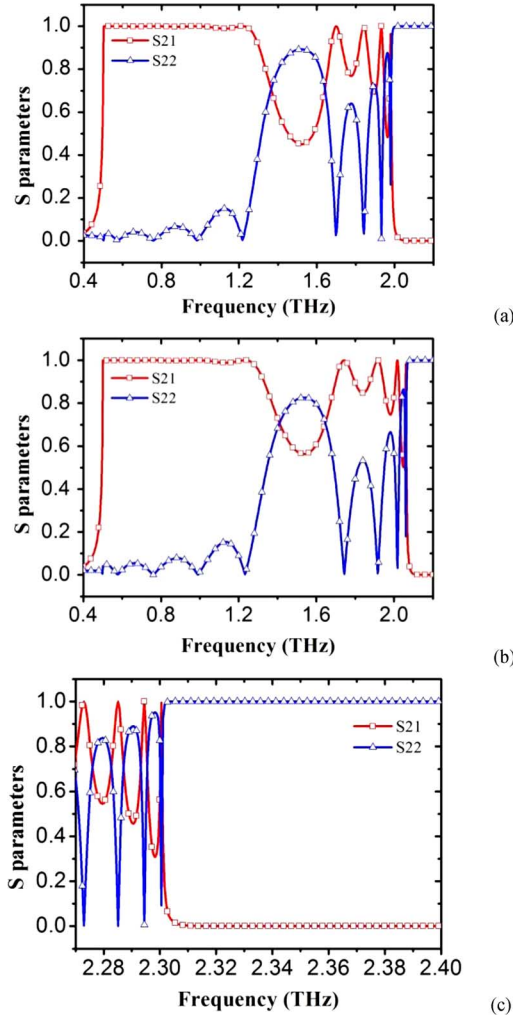


Fig. 7. S-parameters of the DC-SSPP-2 structure: (a) as simulated using our analytical model, (b) as obtained using CST software package, and (c) details around the narrow transmission peak near $f = 2.28$ THz. In these figures, the red line with square data markers denotes the S_{21} parameter, and the blue line with triangle data markers represents the S_{22} parameter.

The existence of sub-wavelength transmission band, and sharp transmission peaks under certain device designs enables us to employ the DC-SSPP structure in various applications such as frequency filters and active switches. Such property is a unique feature of the DC-SSPP structure.

VI. DISCUSSION

From the simulation results demonstrated in the previous two sections, it is fair to conclude that our calculation of both dispersion relationship and S-parameters show a very close match to the result obtained from elaborate simulation software packages (here we use CST). In this section, discussions regarding the small quantitative difference between the numerical results from two approaches will be given out in detail.

In both the result for dispersion curves and that of S-parameters, there are discrepancies in the frequency number where certain curve features lie. For example, when we consider the frequency where the first anti-symmetric mode starts for the DC-SSPP-1 structure, our result shows 1.025 THz while the

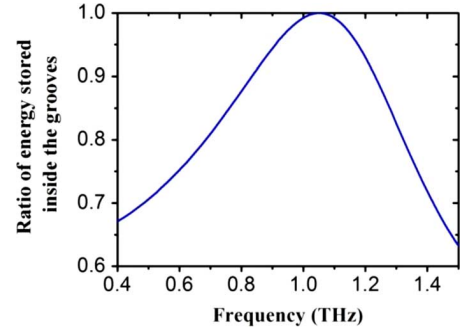


Fig. 8. Percentage of energy stored inside the groove regions as compared with the total EM field energy, plotted against frequencies.

CST simulation suggests 0.963 THz, which demonstrates a difference of 6%.

We conclude such discrepancy to be caused largely by the fact that *edge effect* is not included in our analysis of the structure. In real situations, EM field inside the grooves (namely in Region II in our convention) and outside them (in Region I) are coupled with each other near the boundaries. In other words, the field lines are not strictly horizontal or perpendicular to the boundary when they are crossing it, instead they are bended to ensure a smooth transition between mode profiles in two different regions. This physics phenomenon is called the *edge effect* since they tend to happen at the edge of transitions, and usually become more significant when the wavelength of the EM field becomes smaller, especially when it is comparable with the periodic structural dimensions.

For the DC-SSPP-1 structure, the SSPP resonance frequency at 1.025 THz corresponds to a wavelength of $\lambda = 293 \mu\text{m}$. Although this wavelength is larger than the longitudinal dimension of the structure ($d = 100 \mu\text{m}$), their magnitude are still somewhat comparable. In this case the edge effect can introduce small yet visible errors into our analysis, as the division of mode profiles strictly into two separate regions is not an accurate description of the mode distribution anymore.

The influence is even more significant when the frequency is near the plasmonic resonance frequency, as at resonance most of the energy is localized inside the groove region and the bending of EM field is therefore more emphasized. Fig. 8 illustrates the ratio of energy stored inside the groove as compared with total energy in the DC-SSPP-1 structure. A maximum of the curve can be clearly seen when the frequency is near resonance.

On contrary, if the resonance frequency of the structure is much larger than its periodic dimensions, edge effect will become negligible and the accuracy of our calculation will be improved. As an example, we simulated the structure with $h = 200 \mu\text{m}$, and with all other dimensions staying the same as DC-SSPP-1 structure. In this case, the SSPP resonance frequency of the structure as calculated by (10) has become 0.625 THz, which corresponds to a wavelength $\lambda = 480 \mu\text{m}$. In Fig. 9 the dispersion relationship of the first five modes of such structure is shown, along with the results from the CST simulations. As can be seen, here the results from both approaches are almost identical to each other. For example, the frequency where the first anti-symmetric mode resides is at 0.620 THz in our simulation, while the same frequency point in the CST result is located at 0.613 THz (both in close agreement

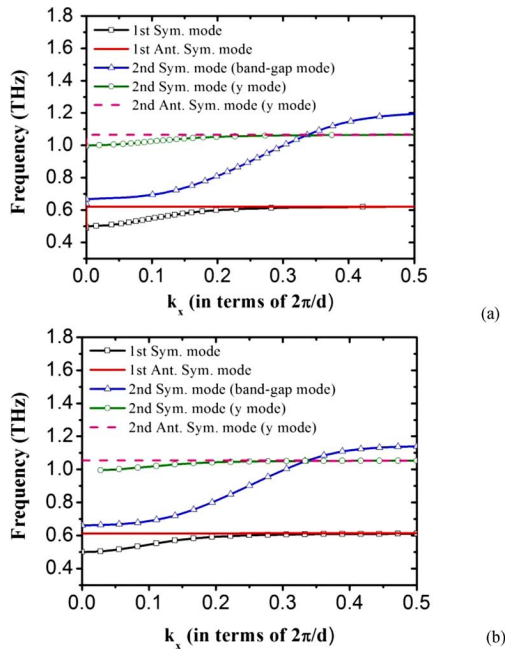


Fig. 9. Dispersion map of the first 5 modes of the DC-SSPP structure using all the other dimensions of the DC-SSPP-1 structure but $h = 200 \mu\text{m}$, (a) as simulated using our analytical model, and (b) as obtained using CST software package.

with our estimation using (26), indicating a diminished error down to 1.1%.

VII. CONCLUSION

In this paper a full analytical model of the doubly corrugated SSPP (DC-SSPP) structure working at THz frequency is established. Simulations based on such model on the dispersion relationships as well as S-parameters of the structure has been carried out, and the results are compared with those obtained by simulations using elaborate industrial level software packages, in this case the CST. It is demonstrated that although we implemented a far less complicated mathematical model to the problem, the result is in general accurate. The shape of different curves coincides with each other very well. A small quantitative error still exists, albeit it is not by any means significant.

Our simulation can be used to calculate dispersion relationships of arbitrary number of SSPP modes in the DC-SSPP structure, therefore providing a full dispersion map of the structure. Discrete transmission bands in sub-wavelength scales have been observed. If the structure is designed properly, a sharp transmission peak in frequency domain is also demonstrated, which can be extremely useful in the design of devices such as passive frequency filters and active THz switches.

Considering the simplicity of our algorithm and fast computing time as a result, the analysis as presented in this paper is an effective method in the initial design stages of any device based on DC-SSPP structures.

ACKNOWLEDGMENT

The authors would like to thank Dr. D. Woolard, who is the ARO Program Manager for encouraging them to develop THz DC-SSPP waveguide structures for biosensing applications.

REFERENCES

- [1] D. M. Mittleman, R. H. Jacobsen, and M. C. Nuss, "T-ray imaging," *IEEE J. Sel. Topics Quantum Electron.*, vol. 2, no. , pp. 679–692, 1996.
- [2] P. H. Siegel, "Terahertz technology," *IEEE Trans. Microw. Theory Techn.*, vol. 50, no. , pp. 910–928, 2002.
- [3] R. Kohler *et al.*, "Terahertz semiconductor-heterostructure laser," *Nature*, vol. 417, pp. 156–159, 2002.
- [4] Y.-M. Shin *et al.*, "Microfabrication of millimeter wave vacuum electron devices by two-step deep-etch x-ray lithography," *Appl. Phys. Lett.*, vol. 88, pp. 091916–3, 2006.
- [5] J. Tucek, D. Gallagher, K. Kreisler, and R. Mihailovich, "A compact, high power, 0.65 THz source," in *2008 IEEE Int. Vacuum Electron. Conf. (IVEC 2008)*, 2008, pp. 16–17.
- [6] Y.-M. Shin *et al.*, "Terahertz vacuum electronic circuits fabricated by UV lithographic molding and deep reactive ion etching," *Appl. Phys. Lett.*, vol. 95, pp. 181505–3, 2009.
- [7] R. Mendis and D. Grischkowsky, "Plastic ribbon THz waveguides," *J. Appl. Phys.*, vol. 88, pp. 4449–4451, 2000.
- [8] W. Zhu, A. Agrawal, and A. Nahata, "Planar plasmonic terahertz guided-wave devices," *Opt. Express*, vol. 16, p. 6216, 2008.
- [9] G. Kumar, A. Cui, S. Pandey, and A. Nahata, "Planar terahertz waveguides based on complementary split ring resonators," *Opt. Express*, vol. 19, p. 1072, 2011.
- [10] G. Gallot, S. P. Jamison, R. W. McGowan, and D. Grischkowsky, "Terahertz waveguides," *J. Opt. Soc. Amer. B*, vol. 17, pp. 851–863, 2000.
- [11] S. P. Jamison, R. W. McGowan, and D. Grischkowsky, "Single-mode waveguide propagation and reshaping of sub-ps terahertz pulses in sapphire fiber," *Appl. Phys. Lett.*, vol. 76, pp. 1987–1989, 2000.
- [12] K. Wang and D. M. Mittleman, "Metal wires for terahertz wave guiding," *Nature*, vol. 432, pp. 376–379, 2004.
- [13] J. B. Pendry, L. Martín-Moreno, and F. J. García-Vidal, "Mimicking surface plasmons with structured surfaces," *Science*, vol. 305, pp. 847–848, Aug. 2004.
- [14] C. R. Williams, S. R. Andrews, S. A. Maier, A. I. Fernández-Domínguez, L. Martín-Moreno, and F. J. García-Vidal, "Highly confined guiding of terahertz surface plasmon polaritons on structured metal surfaces," *Nat. Photon.*, vol. 3, p. 175, 2008.
- [15] A. I. Fernández-Domínguez, E. Moreno, L. Martín-Moreno, and F. J. García-Vidal, "Guiding terahertz waves along subwavelength channels," *Phys. Rev. B*, vol. 79, p. 233104, 2009.
- [16] F. J. García-Vidal, L. Martín-Moreno, T. W. Ebbesen, and L. Kuipers, "Light passing through subwavelength apertures," *Rev. Mod. Phys.*, vol. 82, pp. 729–787, 2010.
- [17] S. H. Kim, T. T. Kim, S. S. Oh, J. E. Kim, H. Y. Park, and C. S. Kee, "Experimental demonstration of self-collimation of spoof surface plasmons," *Phys. Rev. B*, vol. 83, p. 165109, 2011.
- [18] K. Song and P. Mazumder, "Active terahertz spoof surface plasmon polariton switch comprising the perfect conductor metamaterial," *IEEE Trans. Electron Devices*, vol. 56, no. , pp. 2792–2799, 2009.
- [19] K. Song and P. Mazumder, "Dynamic terahertz spoof surface plasmon-polariton switch based on resonance and absorption," *IEEE Trans. Electron Devices*, vol. 58, no. 7, pp. 2172–2176, Jul. 2011.
- [20] B. D. McVey, M. A. Basten, J. H. Booske, J. Joe, and J. E. Scharrer, "Analysis of rectangular waveguide-gratings for amplifier applications," *IEEE Trans. Microw. Theory Techn.*, vol. 42, no. , pp. 995–1003, 1994.
- [21] S. A. Maier, S. R. Andrews, L. Martín-Moreno, and F. J. García-Vidal, "Terahertz surface plasmon-polariton propagation and focusing on periodically corrugated metal wires," *Phys. Rev. Lett.*, vol. 97, p. 176805, 2006.
- [22] Q. Gan, Z. Fu, Y. J. Ding, and F. J. Bartoli, "Ultrawide-bandwidth slow-light system based on THz plasmonic graded metallic grating structures," *Phys. Rev. Lett.*, vol. 100, p. 256803, 2008.
- [23] M. Mineo, C. Paoloni, A. Di Carlo, A. M. Fiorello, and M. Dispenza, "Corrugated waveguide slow-wave structure for THz travelling wave tube," in *2009 Eur. Microw. Conf. (EuMC 2009)*, pp. 842–845.
- [24] R. E. Collin, *Foundations for Microwave Engineering*, 2nd ed. Hoboken, NJ: Wiley-IEEE Press.
- [25] R. Safavi-Naini and R. H. MacPhie, "On solving waveguide junction scattering problems by the conservation of complex power technique," *IEEE Trans. Microw. Theory Techn.*, vol. 29, pp. 337–343, 1981.
- [26] L. Li, "Formulation and comparison of two recursive matrix algorithms for modeling layered diffraction gratings," *J. Opt. Soc. Amer. A*, vol. 13, pp. 1024–1035, 1996.
- [27] Z.-Y. Li and L.-L. Lin, "Photonic band structures solved by a plane-wave-based transfer-matrix method," *Phys. Rev. E*, vol. 67, p. 046607, 2003.



Zhao Xu received the B.S. degree in electronics engineering from Tsinghua University, Beijing, China, in 2006 and the M.S. degree in electrical engineering from the University of Michigan, Ann Arbor, in 2008, where he is currently working toward the Ph.D. degree.

He is a Graduate Student Research Assistant with the Electrical Engineering and Computer Science Department, University of Michigan. His current research interests include the modeling, simulation, and design of THz spoof surface plasmonic structures and components.

tures and components.



Kyungjun Song received the B.S. degree in mechanical engineering from Seoul National University, Seoul, Korea, in 2002 and the M.S. degree in mechanical engineering from the University of Michigan, Ann Arbor, in 2004. He received the Ph.D. from the University of Michigan, Ann Arbor, in 2010.

He is currently a Post-Doctorate with the Department of Electrical Engineering and Computer Science, University of Michigan. His research interests include modeling, simulation, and design

of plasmonic nanoarchitecture.



Pinaki Mazumder (S'84–M'87–SM'95–F'99) received the Ph.D. degree from the University of Illinois at Urbana-Champaign, Urbana, in 1988.

He is currently a Professor with the Department of Electrical Engineering and Computer Science, University of Michigan (UM), Ann Arbor. He is currently on leave for one year from the University of Michigan to serve as the lead Program Director of the Emerging Models and Technologies Program with the U.S. National Science Foundation, Arlington, VA. He was for six years with industrial R&D centers

that included AT&T Bell Laboratories, where in 1985, he started the CONES Project—the first C modeling-based very large scale integration (VLSI) synthesis tool at India's premier electronics company, Bharat Electronics, Ltd., India, where he had developed several high-speed and high-voltage analog integrated circuits intended for consumer electronics products. He is the author or coauthor of more than 200 technical papers and four books on various aspects of VLSI research works. His current research interests include current problems in nanoscale CMOS VLSI design, computer-aided design tools, and circuit designs for emerging technologies including quantum MOS and resonant tunneling devices, semiconductor memory systems, and physical synthesis of VLSI chips.

Dr. Mazumder is a Fellow of the American Association for the Advancement of Science (2008). He was a recipient of the Digital's Incentives for Excellence Award, BF Goodrich National Collegiate Invention Award, and Defense Advanced Research Projects Agency Research Excellence Award.